# ULTRASONIC PARAMETRIC IMAGING: A SYSTEMS APPROACH AND CLINICAL EXAMPLES

**F. L. Lizzi**
Biomedical Engineering Laboratories, Riverside Research Institute, New York, NY USA
lizzi@rrinyc.org

## Abstract

Ultrasonic spectral parameter images offer significant potential for medical applications. They are generated with a sequence of procedures that can affect the accuracy and precision of imaged data. Radio-frequency echo data are analyzed using Fourier transformation and calibration, to remove system artifacts. Local spectra (in dB) are analyzed with linear regression to derive spectral slope and mid-frequency amplitude, each of which is imaged in cross-sectional formats.

These images can be used with other data. Clinical databases can be used to demarcate image regions whose features are consistent with a particular disease (e.g., prostate cancer). Previous patient images can detect responses to therapy. Theoretical models can analyze the imaged parameters to compute and image effective properties (e.g., sizes) of sub-resolution tissue constituents.

This report addresses calibration, system, and processing effects on the accuracy and precision of parametric images; results agree closely with simulations, experiments, and clinical data from various organs.

## Introduction

Ultrasonic spectral parameter images have been explored as a means of extracting tissue information that is not conveyed in conventional ultrasonic images. This report describes parametric images that utilize spectrum analysis of radio-frequency (RF) echo signals to examine backscatter characteristics and to derive underlying tissue properties. Such images have been used to convey morphologic information (e.g., sizes of tissue constituents)[1–4]; to diagnose disease (by using spectral classifiers)[5-8]; to monitor treatment responses [9]; and to elucidate the 3-D morphology of abnormal and diseased structures [10].

Several considerations motivate the use of spectral processing for parametric imaging. Many of the interactions in ultrasonography involve convolution in the time domain, and therefore result in simpler multiplicative operations in the frequency domain. This facilitates compensation for system properties and attenuation in intervening tissue [9,11]. Spectral parametric imaging can also utilize theoretical models of beam propagation and ultrasonic backscatter, which are often formulated in the frequency domain, and tissue properties, which are often measured as functions of frequency. Lastly, power spectra provide a well-established means of accounting for the stochastic aspects of ultrasonic backscatter.

This report briefly reviews the key elements in spectral parameter imaging. First, it describes the processing sequence needed to produce tissue spectra that are calibrated to compensate for extraneous system factors [11,12]. These procedures are used to generate parameter images. They have also been used in a region-of-interest (ROI) mode to establish disease-indexed databases and diagnostic classifiers that can be used in conjunction with parameter images.

Next, theoretical models that provide images of tissue parameters are briefly reviewed. These models permit measured spectral parameters to be interpreted in terms of quantitative estimates of physical tissue parameters. Various morphologies have been analyzed including tissue constituents that are isotropic; quasi-cylindrical, and quasi-planar [13,14]. The models enable estimation of characteristic sizes and "acoustic concentration." The latter parameter is defined as $CQ^2$ where C is the concentration of scatterers and Q describes their relative acoustic impedance with respect to the surround.

The report then presents recent results related to the accuracy and precision of spectral estimates used in ROI and parameter imaging modes. It summarizes recent results obtained for calibration errors that can occur when using planar calibration targets [11]. It then addresses the statistics of parameter estimation in terms of bias and precision. These statistics depend primarily on the bandwidth and degree of spectral resolution. Statistical studies must account for the log operation typically employed in parameter estimations. The accuracy and precision of spectral-parameter estimation are of great importance in all applications; in this regard, special attention must be given to biases that can differ in parametric images and ROI data used for classification.

## Spectral Parameter Images

Spectral parameter images are formed using the same sequence of operations applied in ROI spectrum analysis, which will be described first. For simplicity, we consider linear-scan examinations conducted within the focal zones of single element focused transducers. RF echo data are digitally acquired from scan lines in a conventional ultrasound scan. The ROI is then demarcated on a conventional B-mode image. Its range length L and cross-range width W define the

length of the range gate to be employed and the number of scan-line segments N to be examined [11].

Along each scan-line segment in the ROI, we employ a Hamming gating function of length L to multiply RF echo data prior to Fast Fourier Transformation (FFT). Spectral magnitudes along each line are then squared and averaged to form a power spectrum estimate. This is then divided by a calibration spectrum to remove system artifacts associated with the transfer function of the transducer and associated electronics. Calibration spectra can be obtained from a planar reflector in the transducer's focal plane [11] or from a tissue phantom [3]. Often, planar-reflector data is supplemented with phantom spectral data to compensate for range-dependent diffraction effects outside of the focal zone.

Calibrated power spectra are then expressed in dB for further analysis. Our research employs linear-regression analysis, applied over a bandwidth B that exhibits adequate signal-to-noise ratio (SNR) [5]. We typically summarize spectral features in terms of the midband fit (dB), which is the regression-line value at the center frequency of B, and the spectral slope (dB/MHz). (Midband fit is numerically related to integrated backscatter [16].) We sometimes employ the spectral intercept (extrapolation to zero frequency). This intercept is not independent of the other parameters; as described below, its advantage lies in being insensitive to intervening attenuation.

Parameter images are formed in a similar manner [1,5]. A sliding gate function (Hamming) is used to compute calibrated spectra as well as midband fit and slope along local segments in each scan line. (Cross-range averaging is usually not applied so that N=1.) Local values of M (midband fit) and s (slope) are both encoded as gray-scale or color-coded parameter images. Figure 1 shows an example of a midband fit image of a metastatic carcinoma in liver.

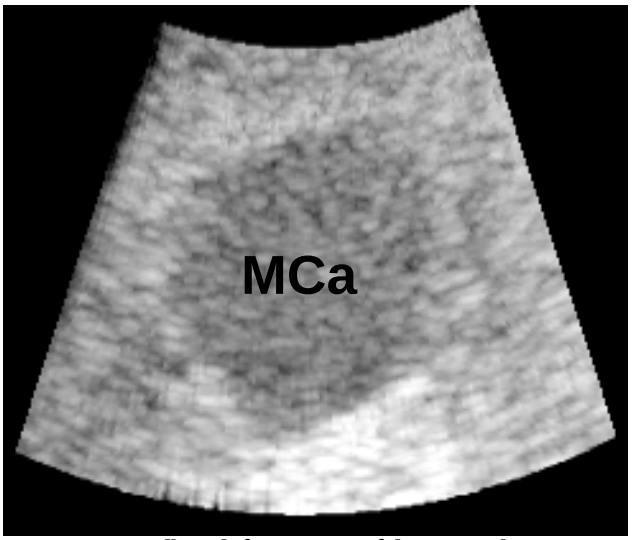


Figure 1: Midband fit image of liver with metastatic carcinoma (MCa) ; 3-MHz center frequency.

Attenuation in intervening tissues affects these images. If the attenuation coefficient is constant and equal to $\alpha$ (dB/MHz-cm), then the imaged values of M and s are:

$$M' = M - 2\alpha x f_c \quad ; \quad s' = s - 2\alpha x \qquad (1)$$

where the primes denote imaged parameters, $f_c$ is the center frequency, and x is tissue depth [9]. These attenuation effects are easily corrected if $\alpha$ is known or estimated. The measured intercept value is equal to $M' - s'f_c$ which is seen to equal $M - sf_c$; thus, intercept is not affected by attenuation under these conditions.

**Tissue Parameter Images**

The preceding description applied to the imaging of spectral parameters, which describe signal features. Several groups have applied theoretical models to backscatter spectra in order to estimate and image tissue parameters, which are properties of microstructure rather than of echo signals [2-4, 13].

Most tissues of interest are stochastic due to random fluctuations in the properties and positions of their constituents. It is often assumed that these microstructures present acoustic impedance distributions that are statistically homogeneous with wide sense stationarity. Further assumptions are made about morphology so that appropriate spatial autocorrelation functions (ACF) can be specified. Isotropic scatterers have been analyzed with radially symmetric ACF's that apply to spherical scatterers; radially symmetric exponential and Gaussian ACF's have also been analyzed [13], with most emphasis on the latter.

We have shown that each of these isotropic scatterers produces the same slope, intercept, and, by implication, midband fit values when their effective radii are smaller than the wavelength at $f_c$ [13]. We concluded the Gaussian ACF was most appropriate for many tissues because it produces negative slopes for larger scatterer sizes; such negative slopes have been seen in a variety of tissues, and they are not predicted by the spherical or exponential model.

Insana et al [2] have employed a Gaussian ACF and developed a procedure for estimating the effective sizes of constituent scatterers by analyzing spectral shape. Our laboratories have shown that spectral slope estimates can be used to estimate scatterer sizes. Using a 3-D Gaussian ACF, we have derived a pair of closed-form relations that permits the effective scatterer radius $\rho$ to be estimated from s and also permit values of $CQ^2$ to be estimated from M and s [5, 14].

The models described above can be applied to ROI spectra to build disease-indexed databases and to develop disease classifiers. They can also be applied

to spectral parameter images (M and s) to synthesize images of ρ and $CQ^2$.

In 40-MHz ocular examinations, we have recently found that $CQ^2$ levels are distinctly different in subsegments of the anterior chamber. This has permitted us to develop segmentation algorithms to generate cogent 3-D images from parallel plane data. Figure 2 shows a gray-scale reproduction of a segmented 3-D image that employed different colors to depict the iris (I), sclera (S), ciliary body muscles (CM) and ciliary processes (CP). The viewpoint is within the globe. Such data are now being used to measure the configurations and volumes of these structures in normal and glaucomatous eyes.

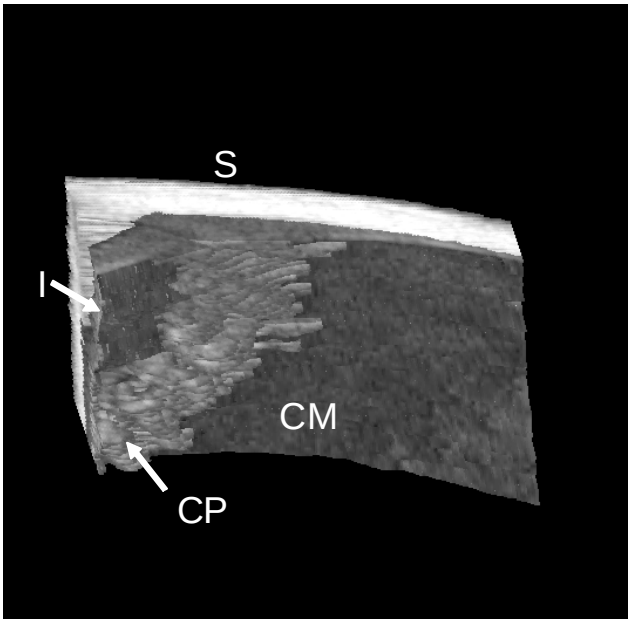


Figure 2: Segmented 3-D image of anterior eye.

**Analysis of Calibration and Spectral Statistics**

The accuracy and precision of spectral estimates are critical factors for ROI and parametric imaging modes of analysis. Systematic inaccuracies and statistical biases can cause errors in tissue classification and hinder the use of ROI data for classifying parameter image data. Precision affects the reliability of classification and the degree of variance in spectral parameter images.

The following sections summarize results of recent investigations regarding these issues [15]. First, they describe calibration errors that can arise with planar targets and also describe correction factors that can be applied when needed. Second, they describe phantom and simulation experiments that verified our findings regarding estimator bias and precision in ROI and parametric imaging modes.

Calibration procedures are intended to measure the spectral function $p_0(\omega)$, which is the spectrum of the launched pulse as modified by the transfer function of the electronic receiver [11]. The desired spectrum is frequently measured using the spectrum of RF echoes from a planar reflective surface. This is placed in the transducer's focal plane and viewed at normal incidence. We have shown that this procedure is adequate for narrow beams whose wavefronts match the planar reflective surface [11]. We have recently analyzed this procedure to determine when this condition is satisfied and to derive correction factors that can be employed when it is not fulfilled.

The analysis [15] uses the expression for the focused two-way beam profile in the focal plane, where the axial distance x from the transducer vertex is equal to the focal length F. The received spectrum for a reflection coefficient of unity is then (aside from a phase shift term)

$$p_c(w) = \left(q^2 / p\right) p_0(w) \int_0^\infty \frac{2J_1(2qr)}{2qr} \exp\left(-j\frac{2qr^2}{a}\right) 2p\ r\ dr \qquad (2)$$

where $q = \omega a/2cF$ ; $\omega$ is radian temporal frequency, c is the speed of propagation, r is radial off-axis distance, and a is the transducer radius. $J_1$ represents a first-order Bessel function.

The ratio $K = p_c(\omega) / p_0(\omega)$ can be evaluated from this expression as:

$$K = 1 - (J_0(qa) - j\ J_1(qa)) \exp(jqa) \qquad (3)$$

where j represents the square root of -1 and $J_0$ is a zero-order Bessel function.

The magnitude of this result is plotted in Fig. 3. In the ideal case, the ratio $p_c(\omega) / p_0(\omega)$ would be unity (0 dB). Figure 3 shows that this result is approached only as q approaches infinity. Eq. 3 can provide correction factors for practical situations. This can be done by evaluating it over the bandwidth to be analyzed, using the transducer parameters a and F. The measured value of $p_c(\omega)$ can then be divided by the result to compensate for departures from the ideal case. In addition, the result can be stated in dB and analyzed with linear regression techniques to compute (and correct) errors in estimates of M and s. For a typical ocular transducer ( a = 5 mm; F = 35 mm; 5-15 MHz band), the midband fit error is - 1.3 dB and the spectral slope error is 0.07 dB/MHz.

**Spectral Statistics**

Several groups have investigated statistical issues related to ultrasonic spectral estimation [3,4,17,18]. We have recently expanded our previous analyses of spectral statistics [19,20] and conducted simulation and phantom studies to verify key results [15]. This report compares simulation and experimental results

with our previous statistical results regarding estimator bias and precision.

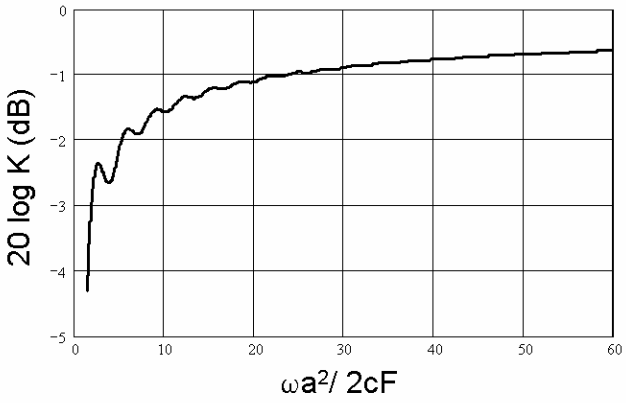


Figure 3 : Spectral ratio (dB) for planar calibration target.

Our theoretical analysis treats the situation in which many independent scatterers with uniformly random positions lie within the gated volume. In this case, RF echoes exhibit a Gaussian probability density function (pdf) and power spectrum estimates for a particular frequency $f_m$ exhibit a Chi-square pdf before conversion to dB. When converted to dB, the power spectrum exhibits a double-exponential pdf [20].

For single-line power spectra, (N=1), that are normalized to their mean value at each frequency, the Chi-square pdf has the form exp(-S) where the positive variable S is the normalized spectral value. The corresponding pdf for w = 10 log S is

$$g(w) = \frac{1}{4.34}\exp\left[\frac{w}{4.34} - \exp\left(\frac{w}{4.34}\right)\right] \quad (4)$$

Under these conditions, our results showed that a bias exists in the average midband fit values estimated from parameter images (N=1) compared to the unbiased result obtained using an ROI mode in which N, the number of averaged spectra, is large (e.g., N > 10). The bias arises because the ROI mode first estimates mean spectral levels, $\mu_m$ at frequency $f_m$, before conversion to dB. The value of $\mu_m$ is an unbiased estimate of spectral power which, upon conversion to dB, is 10 log $\mu_m$. In contrast, parameter images process unaveraged values of spectra expressed in dB. The corresponding expected value at $f_m$ (for N=1) was found to be 10 log $\mu_m$ - 2.5 dB [19,20].

These results show that the mean spectral values at all frequencies are 2.5 dB lower in the parameter image mode. Since this bias affects all frequencies, it will correspondingly reduce midband fit values in parameter images with respect to those in ROI analyses. Spectral slope values will not differ because spectral shapes are not affected.

Our analyses [19,20] also derived expressions for the standard deviations of midband fit ($\sigma_M$) and slope ($\sigma_s$) when a Hamming window of length L (mm) is employed over a bandwidth B (MHz); assuming a propagation velocity of 1,550 m/s:

$$s_M = \frac{s}{\sqrt{BL}} \quad (5a)$$

$$s_s = \frac{\sqrt{12}\, s\, \sqrt{BL}}{B\sqrt{B^2L^2 - 1}} \quad (5b)$$

$$s_s \approx \frac{\sqrt{12}\, s}{B\sqrt{BL}};\ B^2L^2 >> 1 \quad (5c)$$

where $\sigma$ = 5.6 dB for the parameter image mode and $\sigma$ = 4.34 dB for the ROI mode (N >10).

We have now expanded these findings and verified them using numerical simulations and experimental measurements in tissue phantoms.

The simulations and experiments both involved a 10-MHz transducer (a = 5 mm; F = 50 mm) whose -15 dB bandwidth was 10 MHz (5- to 15-MHz range). The simulated transducer was assigned a Gaussian function $p_0(\omega)$ with this bandwidth; the experimental transducer (Panametrics, Inc., Waltham, MA) was calibrated using a planar calibration target. Simulated scatterers had Gaussian impedance profiles with an effective radius of 5 μm, a concentration of 110 particles/mm$^3$, and uniformly random positions throughout the analyzed region. Experiments utilized a tissue-mimicking phantom (ATS Laboratory, Bridgeport, CT) consisting of a rubber block (8 x 3 x 5 cm) with a propagation speed of 1,450 m/s and an attenuation coefficient of 0.5 dB/MHz-cm. The block contained a random distribution of glass beads with a mean radius of 5.1+/-1.2 μm and a concentration of 1.28 x $10^5$ particles/ mm$^3$. The block was linearly scanned and RF data were acquired using a model 9400C analog-to-digital converter unit (LeCroy Corporation, Chestnut Ridge, NY).

To examine spectral pdfs for the phantom, we divided the power spectrum measured along each scan line by the average power spectrum. We then computed the composite histogram of normalized spectral values from frequencies spaced at 0.5 MHz intervals between 5 and 15 MHz. The result, shown in Figure 4A, shows excellent agreement with the Chi-square pdf (negative exponential) described above. We then converted the normalized spectra to dB and re-evaluated the pdf. As seen in Fig. 4B, the result is in excellent agreement with the double exponential pdf of eq. 4.

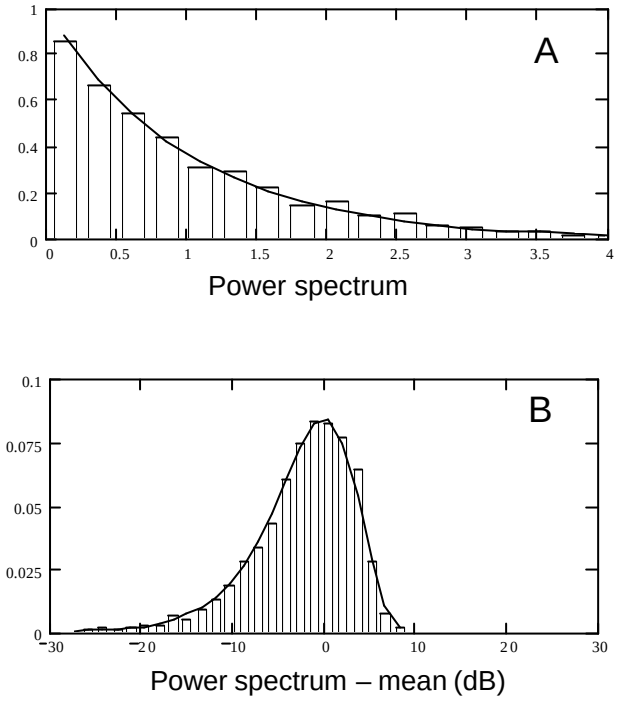


Figure 4 : Histograms (bars) of normalized phantom spectra before (A) and after (B) conversion to dB. Solid curves are theoretical probability density functions.

The bias in midband fit values was calculated by subtracting the mean ROI value (N=10) from the average parameter-image mode value. The simulation result was -2.33 dB and the phantom result was -2.0 dB; both are within 0.5 dB of the theoretical -2.5 dB.

Table 1 shows simulation results for the standard deviations of midband fit estimates in the ROI mode (N=10) and the parameter imaging mode (N=1). It also shows results for spectral slope in each mode. In all cases, excellent agreement is seen with theory.

Table 1 : Standard deviations for spectral parameters.

| Parameter | N | Simulation | Theory |
|---|---|---|---|
| Midband fit dB | 1 | 1.26 | 1.25 |
| | 10 | 0.36 | 0.32 |
| Spectral slope dB/MHz | 1 | 0.45 | 0.43 |
| | 10 | 0.11 | 0.11 |

We also determined $\sigma_M$ and $\sigma_s$ as a function of bandwidth for the parameter imaging mode. Our goal was to verify the different dependencies on bandwidth in eq. 5. As seen in Figs. 5 and 6, both the simulation and experimental curves followed the theoretical results very closely.

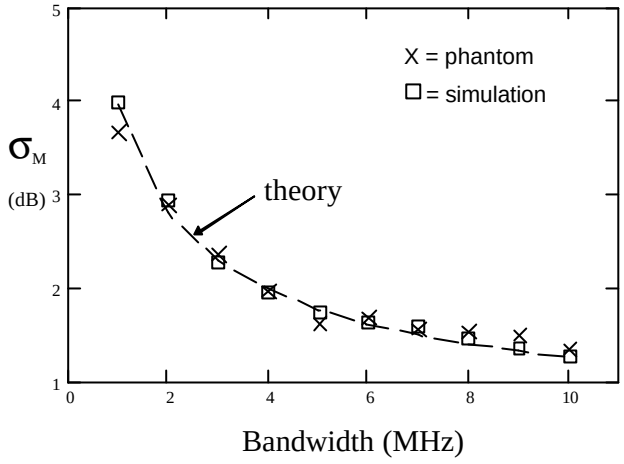


Figure 5 : Standard deviation of midband fit vs. bandwidth for phantom and simulations.

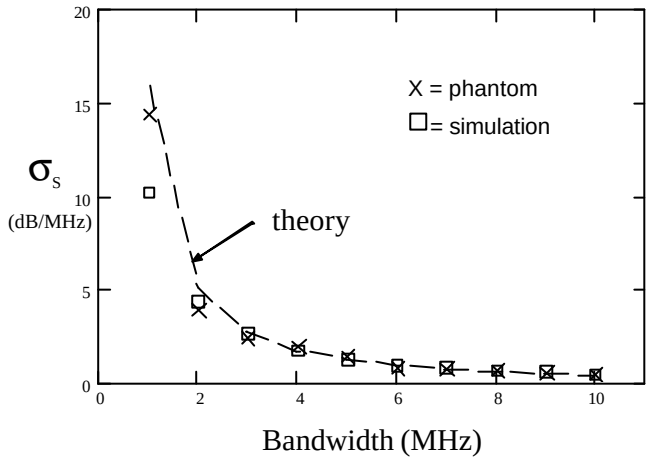


Figure 6 : Standard deviation of spectral slope vs. bandwidth for phantom and simulations.

**Comparison with Previous Clinical Results**

We compared results for spectral parameter standard deviations (eq. 5) with representative data (obtained with Hamming gate functions) from previous clinical examinations of several organs. These examinations had been conducted in our research programs using digital RF acquisition from a variety of scanners with a range of center frequencies. They included the liver (3 MHz), prostate (7 MHz), breast (7.5 MHz), and eye (10 MHz). The standard deviations of midband fit and spectral slope were determined by analyzing regions within one to three spectral parameter images (N=1) of each organ, using techniques described in a previous report [20]. In each image, the analysis region was placed in an area whose properties were visually judged to be homogeneous (i.e., not near boundaries or abrupt variations in gray scale texture). Each area contained at least 3 x 3 independent samples that were separated by L/2 in range and a half

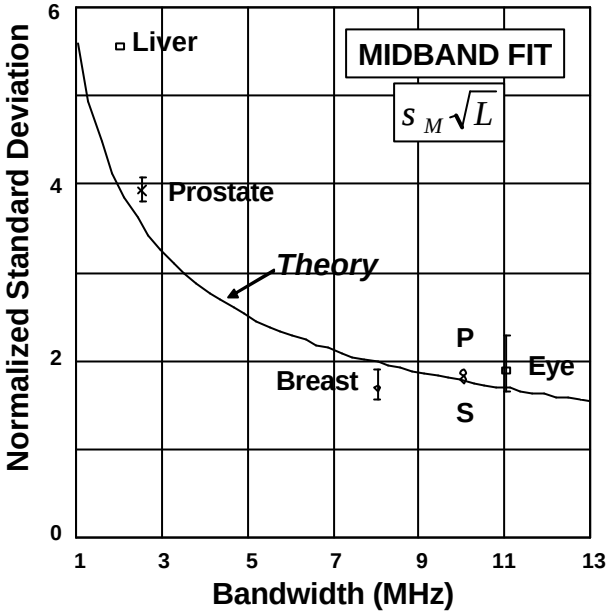


Figure 7 : Normalized standard deviations of midband fit.

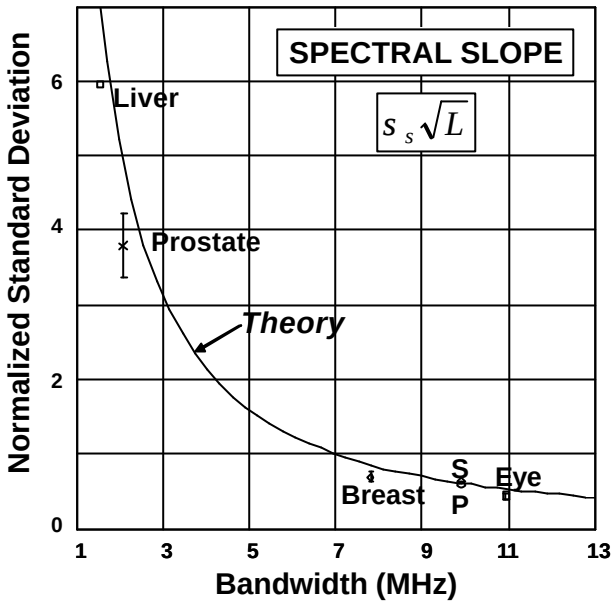


Figure 8 : Normalized standard deviations of spectral slope.

beam width in cross-range.

To compare these results with the theoretical results of eq. 5a and 5c, we multiplied the computed and theoretical standard deviations by $L^{1/2}$ and plotted them as a function of bandwidth. (L ranged from 1 to 10 mm.) Figure 7 plots results for midband fit; the bars represent the range of values found in each subject. The figure also plots the phantom (P) and simulation (S) results from the current study. The results are seen to follow the theoretical expression closely over bandwidths ranging from 2 to 11 MHz. Figure 8 shows corresponding results for spectral slope ( $\sigma_s$ $L^{1/2}$); these also demonstrate close agreement with theory.

**Summary**

Parametric images can provide cogent tissue descriptors in terms of spectral parameters (midband fit, slope) and derived property estimates (size, $CQ^2$). The accuracy and precision of these depends upon several factors. Calibration using planar targets can introduce errors if $\omega a/2cF$ is not much larger than unity. In such cases, eq. 3 can be used to compute spectral deviations from the ideal so that the calibration spectrum and spectral parameters can be corrected.

Our analysis of spectral statistics is applicable to tissues containing many (> 10) independent random scatterers in L. The analysis showed that a constant bias of -2.5 dB occurs in unaveraged spectra expressed in dB compared to ROI spectra that are averaged from a large number of scan lines before dB conversion. The same bias appears in estimates of midband fit and integrated backscatter, and it therefore affects $CQ^2$ estimates. The bias must be corrected before ROI databases are used to classify tissues in parameter images. (Our more recent analysis [15] describes the bias as a function of N.) The bias does not affect spectral shape, estimates of spectra slope, or derived estimates of scatterer size.

The precision of spectral parameter estimates depends upon the bandwidth B and gate-length L. The standard deviations for midband fit are inversely proportional to $(BL)^{0.5}$. The standard deviations for spectral slope are proportional to $B^{1.5}L^{0.5}$ when $(BL)^2>>1$. Thus, bandwidth is particularly important for precise slope estimates.

These standard deviations follow the same dependence on B and L for both ROI and parameter-image modes. However, both standard deviations are smaller by the factor 4.34/5.6 = 0.78 for the ROI mode.

The theoretical results for estimator biases and standard deviations were verified using results from simulations, phantoms, and clinical parameter images obtained over a broad range of center frequencies and bandwidths. The clinical results employed subjective judgments to select statistically homogeneous analysis regions. Nevertheless, they demonstrated excellent agreement with theory over a diverse range of examination parameters.

Overall, the results of this paper can be employed for designing and correcting calibration procedures, selecting processing parameters, and correcting biases so that ROI data can be used to interpret spectral

parameter images. In the future, departures from the predicted statistics may provide information about the degree of statistical heterogeneity and sparseness of scatterers within analyzed tissue regions.

**Acknowledgement**

This research was supported in part by Research Grant EB000238 awarded by the National Institute of Biomedical Engineering and Bioengineering.

**References**

[1] E.F. Feleppa *et al.,* "Diagnostic spectrum analysis in ophthalmology: a physical perspective," Ultrasound Med. Bio., vol. 12, pp. 623-631, 1986.

[2] M.F. Insana and D.G. Brown, "Acoustic scattering theory applied to soft biological tissues," in Ultrasonic Scattering in Biological Tissues, CRC Press, Boca Raton, pp. 75-124, 1993.

[3] A. Gerig *et al.*, "Statistics of ultrasonic scatterer size estimation with a reference phantom," J. Acoust. Soc. Am., vol. 113, pp. 3430-3437, 2002.

[4] M.L. Oelze and W.D. O'Brien, "Method of improved scatterer size estimation and application to parametric imaging using ultrasound," J. Acoust. Soc. Am., vol. 112, pp. 3035-3063, 2002.

[5] F.L. Lizzi *et al.*, "Ultrasonic spectrum analysis for tissue evaluation," Pattern Recognition Letters, vol. 24, pp. 637-658, 2003.

[6] S.L. Bridal *et al.*, "Parametric (integrated backscatter and attenuation) images constructed using backscattered radio frequency signals from human aortae *in vitro*," Ultrasound Med. Bio., vol. 23, pp. 215-229, 1997.

[7] E.F. Feleppa *et al.*, "Spectrum analysis and neural networks for imaging to detect and treat prostate cancer," Ultrason. Imag., vol. 23, pp. 135-146, 2001

[8] S.K. Alam *et al.*, "Computer aided diagnosis of breast lesions using a multi-feature analysis procedure," in Medical Imaging 2002: Ultrasonic Imaging and Signal Processing, Society of Photo-Optical Instrumentation Engineers (SPIE), vol. 4687, pp. 296-303, SPIE, Bellingham WA, 2002.

[9] F.L. Lizzi *et al.*, "Ultrasonic spectrum analysis for tissue assays and therapy evaluation," Int. J. Imaging Syst. Technol., vol. 8, pp. 3-10, 1997.

[10] R.H. Silverman *et al.*, "Three-dimensional high-frequency ultrasonic parameter imaging of anterior segment pathology," Ophthalmology, vol. 102, pp. 837-843, 1995.

[11] F.L. Lizzi *et al.*, "Theoretical framework for spectrum analysis in ultrasonic tissue characterization," J. Acoust. Soc. Am., vol. 73, pp. 1366-1373, 1983.

[12] T.D. Mast and R.C. Waag, "Wave space resolution in ultrasonic scattering measurements," J. Acoust. Soc. Am., vol. 96, pp. 3050-3058, 1995.

[13] F.L. Lizzi *et al.*, "Relationship of ultrasonic spectral parameters to features of tissue microstucture," IEEE Trans. Ultrason. Ferroelect. Freq. Contr., vol. 34, pp. 319-329, 1987.

[14] F.L. Lizzi *et al.*, " Ultrasonic spectrum analysis of different scatterer morphologies; theory and very high frequency clinical results," in Proceedings of the 1996 IEEE Ultrasonics Symposium, pp. 1155-1159, IEEE, New York. (e-mail F.L. Lizzi for typographical corrections.)

[15] F.L. Lizzi *et al.*, "A statistical model for ultrasonic parametric imaging using spectrum analysis," in review.

[16] M. O'Donnell *et al.*, "Broadband integrated backscatter: an approach to spatially localized tissue characterization *in vivo*," in Proceedings of the 1979 IEEE Ultrasonics Symposium, pp. 175-178, IEEE, New York.

[17] P. Chaturvedi and M.F. Insana, "Error bounds on ultrasonic scatterer size estimates," J. Acoust. Soc. Am., vol. 100, pp. 392-399, 1996.

[18] H.J. Huisman and J.M. Thijssen, "Precision and accuracy of acoustospectrographic parameters," Ultrasound Med. Bio., vol. 22, pp. 855-871, 1996.

[19] F.L. Lizzi *et al.*, "Statistics of ultrasonic spectral parameters for liver and prostate examinations," IEEE Trans. Ultrason. Ferroelect. Freq. Contr., vol. 44, pp. 935-942, 1997.

[20] F.L. Lizzi *et al.*, "Statistical framework for ultrasonic spectral parameter imaging," Ultrasound Med. Bio., vol. 23, pp. 1371-1382, 1997.